

Article

Integration of Optical and SAR Data for Burned Area Mapping in Mediterranean Regions

Daniela Stroppiana ^{1,*}, Ramin Azar ^{1,2}, Fabiana Calò ³, Antonio Pepe ³, Pasquale Imperatore ³, Mirco Boschetti ¹, João M. N. Silva ⁴, Pietro A. Brivio ¹ and Riccardo Lanari ³

¹ Institute for Electromagnetic Sensing of the Environment, Italian National Research Council, Via Bassini 15, 20133 Milan, Italy; E-Mails: azar.r@irea.cnr.it (R.A.); boschetti.m@irea.cnr.it (M.B.); brivio.pa@irea.cnr.it (P.A.B.)

² Department of Civil and Environmental Engineering (DICA), Politecnico di Milano, Piazza L. da Vinci 32, 20133 Milan, Italy

³ Institute for Electromagnetic Sensing of the Environment, Italian National Research Council, Via Diocleziano 328, 80127 Napoli, Italy; E-Mails: calo.f@irea.cnr.it (F.C.); pepe.a@irea.cnr.it (A.P.); imperatore.p@irea.cnr.it (P.I.); lanari.r@irea.cnr.it (R.L.)

⁴ Forest Research Centre, School of Agriculture, University of Lisbon, Tapada da Ajuda, 1349-017 Lisbon, Portugal; E-Mail: joaosilva@isa.ulisboa.pt

* Author to whom correspondence should be addressed; E-Mail: stroppiana.d@irea.cnr.it; Tel.: +39-02-23699-297; Fax: +39-02-23699-300.

Academic Editors: Ioannis Gitas and Prasad S. Thenkabail

Received: 4 May 2014 / Accepted: 12 January 2015 / Published: 26 January 2015

Abstract: The aim of this paper is to investigate how optical and Synthetic Aperture Radar (SAR) data can be combined in an integrated multi-source framework to identify burned areas at the regional scale. The proposed approach is based on the use of fuzzy sets theory and a region-growing algorithm. Landsat TM and (C-band) ENVISAT Advanced Synthetic Aperture Radar (ASAR) images acquired for the year 2003 have been processed to extract burned area maps over Portugal. Pre-post fire SAR backscatter temporal difference has been integrated with optical spectral indices to the aim of reducing confusion between burned areas and low-albedo surfaces. The output fuzzy score maps have been compared with reference fire perimeters provided by the Fire Atlas of Portugal. Results show that commission and omission errors in the output burned area maps are a function of the threshold applied to the fuzzy score maps; between the two extremes of the greatest producer's accuracy (omission error < 10%) and user's accuracy (commission error < 5%),

an intermediate threshold value provides errors of about 20% over the study area. The integration of SAR backscatter allowed reducing local commission errors from 65.4% (using optical data, only) to 11.4%, showing to significantly mitigate local errors due to the presence of cloud shadows and wetland areas. Overall, the proposed method is flexible and open to further developments; also in the perspective of the European Space Agency (ESA) Sentinel missions operationally providing SAR and optical datasets.

Keywords: Landsat TM; Synthetic Aperture Radar (SAR); fuzzy sets theory; fire monitoring; burned area mapping

1. Introduction

Forest fires in the Mediterranean and Temperate Continental zones of Europe have strong ecological and socio-economic impacts [1]. The application of improved and integrated monitoring tools is therefore of crucial importance to assess and understand the effects of annually-occurring forest fires. It is nowadays possible to observe long-term global and regional changes from several imaging systems onboard satellite platforms, continuously monitoring our planet's surface, including sensors operating in different regions of the electromagnetic spectrum. The different methodologies and techniques developed to study biomass, and more specifically burned areas, can be categorized according to the investigated spectral portion (*i.e.*, visible, infrared and microwave).

As far as the optical and infrared imaging sensors are concerned, several techniques have been exploited to map burned areas [2–8]. In particular, large-scale studies have relied on the availability of coarse resolution satellite data, such as NOAA-AVHRR (National Oceanic and Atmospheric Administration/Advanced Very High Resolution Radiometer) [2–4], SPOT-VGT (Satellite Pour l'Observation de la Terre/VEGETATION) [9,10], NASA-MODIS (National Aeronautics and Space Administration-Moderate Resolution Imaging Spectrometer) [11] and the geostationary Meteosat Visible and InfraRed Imager (MVIRI)/Spinning Enhanced Visible and InfraRed Imager (SEVIRI) satellites [12], as well as the Geostationary Operational Environmental Satellites (GOES) [13], offering the advantage of multi-temporal and frequent acquisitions. These imaging sensors provide frequent acquisitions, thus supporting the implementation of image differencing techniques that can enhance the separability between burned and unburned areas. In Mediterranean Europe, where burned areas can be small and very fragmented, regional scale studies [5] require medium to high spatial resolution satellite images. Landsat TM/Enhanced TM plus (ETM+) data have therefore largely been used [6–8] thanks to their suitable geometric and spectral characteristics for mapping areas affected by fires. Nonetheless, analyses based on the exclusive use of optical images can be limited by weather conditions (*e.g.*, cloud cover) and errors due to spectral overlaps [9]. Cloud cover can drastically reduce the observation frequency in the visible/infrared domain, which, combined with low fire severity and fast vegetation re-growth after the fire, might result in a low spectral separability between burned and unburned surfaces. Moreover, the spectral confusion of burned areas with dark soils, water surfaces, and shaded regions are still unsolved issues for the optical domain [14], thus reducing the fire mapping capability.

On the other hand, active microwave sensors, and, in particular, Synthetic Aperture Radar (SAR) sensors, generally provide information about both the geometrical (morphology, roughness, *etc.*) and dielectric properties of the surface and subsurface structure of the observed scene. Active microwave sensors do not require “optical visibility” and are not sensitive to weather conditions or cloud cover. Therefore, SAR sensors provide valuable information to complement and enhance multi-spectral observations for fire mapping [15–29].

The occurrence of a fire can change the physical and structural characteristics of the vegetated landscape, thus producing significant variations of its electromagnetic response. Indeed, the physical modifications in the vegetation layer depend on the pre-fire vegetation characteristics, the fire intensity and the weather conditions at the time of fire occurrence, leading, in extreme cases, to (partial) soil exposure. When a fire damages vegetation, the contribution to the total backscattering pertinent to volumetric scattering (taking place within the vegetation layer) decreases, making the contribution related to the scattering from the soil more prominent [30]. In this scenario, the radar signature is strongly affected by variations in soil moisture, depending on the weather and the soil drainage conditions [30–35]. Clearly, the changes in the amount of total backscatter depend on the operative wavelength: while scattering in X-band is predominantly due to the upper part of the vegetation structure, the penetration depth associated with the L-band implies a more significant interaction with the inner structure of the vegetated layer and the vegetation-soil interface [30–32]. Dependency on local topography and polarization has also been observed and linked to the change in the predominant scattering mechanisms [23,36–40].

Despite the preliminary investigations on the potential of (X-, C- and L-band) SAR for burned areas mapping conducted in tropical, boreal and semi-arid ecosystems [17,20–24,41–43], the obtained results are often site-specific and, generally, not directly comparable. In addition to this, no consolidated methodology is available. Indeed, a rigorous approach to comprehensively capture complex soil and vegetation (geo-/bio-physical) variability associated with vegetation fires, should rely on accurate scattering models [30–35]. Although recent studies have been proposed [44], the specific applicability of the available microwave scattering models has not been fully assessed in this context. Accordingly, empirical models are typically employed [15–19].

In boreal regions, earlier studies carried out with C-band ERS (European Remote Sensing) and RADARSAT data have highlighted a general increase in SAR backscattering over burned areas, as a consequence of exposed rough surface and increased soil moisture, mainly due to decreased surface albedo, permafrost melting and lowered evapotranspiration [15,20,21]. For the Mediterranean region, distinct studies have been conducted for the identification of fire perimeters with C-band RADARSAT-1 [32], ERS SAR [24] data on Central Portugal, and L-band ALOS PALSAR (Advanced Land Observing Satellite Phased Array L-band Synthetic Aperture Radar) images on Greece [27]. The potential of SAR data to assess burn severity, fire damage and vegetation recovery has also been investigated [18,19,25,26]. The integration of optical and SAR data for burned area mapping has been addressed only in a few works [28,29,45], despite the recognition of their complementary character [28].

The aim of this paper is to investigate how the distinctive features of the information conveyed by optical and SAR data can be combined to identify burned areas, specifically through the development of an integrated multi-source framework for burned area maps production based on a fuzzy algorithm. This framework is an extension of the automated algorithm originally proposed for Landsat

TM/Enhanced TM plus (ETM+) data, based on the use of fuzzy sets theory and a region growing algorithm [46,47]. This paper is mainly focused on the study of Mediterranean-type regions, particularly on Portugal, affected by remarkable fire events during the year 2003. It is worth remarking that Portugal has been chosen being one of the few countries provided with operational programs for the systematical mapping of burned areas [8]. A multi-temporal analysis (including pre- and post-fire acquisitions) has been conducted by employing both Landsat-5 TM and (C-band) ENVISAT ASAR data to properly integrate the optical indices and scattering signature into the considered fuzzy algorithm to exploit the complementary features of optical and SAR information. Burned area maps have been derived and compared to fire perimeters from the fire atlas available for Portugal, covering the period from 1975 to 2009 and derived from Landsat imagery, to evaluate the contribution of SAR-derived information.

2. Study Area

Figure 1 shows the area covered by the optical and SAR datasets acquired for this study. Portugal is one of the southern European countries most affected by fires, however, with a large temporal and spatial variability of the number of fires and the areas burned. Climate is a major driver of this inter-annual variability to the extent of the burned surface [48,49]. The northern and central parts of the country are much more fire prone than the southern part due to differences on land use and cover, topography, climate and population density [49–51]. With the exception of the flat, coastal region, the highest incidence of burned areas is registered in central Portugal, showing a rugged topography and vegetation cover dominated by forest stands of *Pinus pinaster*, *Eucalyptus globulus* and by shrublands. In contrast, southern Portugal has a flat landscape, dominated by agroforestry systems of *Quercus suber*, *Quercus rotundifolia* woodlands and agricultural fields of cereal crops. Only the southwestern part, characterized by the presence of mountains and a vegetation cover dominated by forest stands of *Eucalyptus globulus* and *Quercus suber*, is affected by wildfires. The study of Oliveira *et al.* [50] revealed fire intervals shorter than 25 years in regions located in the north and centre of the country, contrasting with intervals longer than 50 years in the south. Since the beginning of Forest Service burned area mapping, the year 2003 results as the most affected by wildfires, with more than 425 000 ha of forest and scrublands consumed by fire.

3. Datasets and Pre-Processing

3.1. Landsat TM Images

Five Landsat-5 TM scenes were acquired to cover Portugal (Figure 1) on clear sky dates in late summer 2003; details on the optical TM dataset are given in Table 1, also providing, for each frame, the percentage of area covered by forest according to the Corine Land Cover map [52]. Landsat-5 TM images have been obtained from the USGS Glovis archive [53] as Standard Terrain Correction products (Level 1T -precision and terrain correction) and processed for radiometric calibration and atmospheric correction with the 6S code [54]. Surface reflectance in the visible, near-infrared and shortwave infrared wavelength domains has been used as input data into the fuzzy burned area mapping algorithm, as described in Section 4.

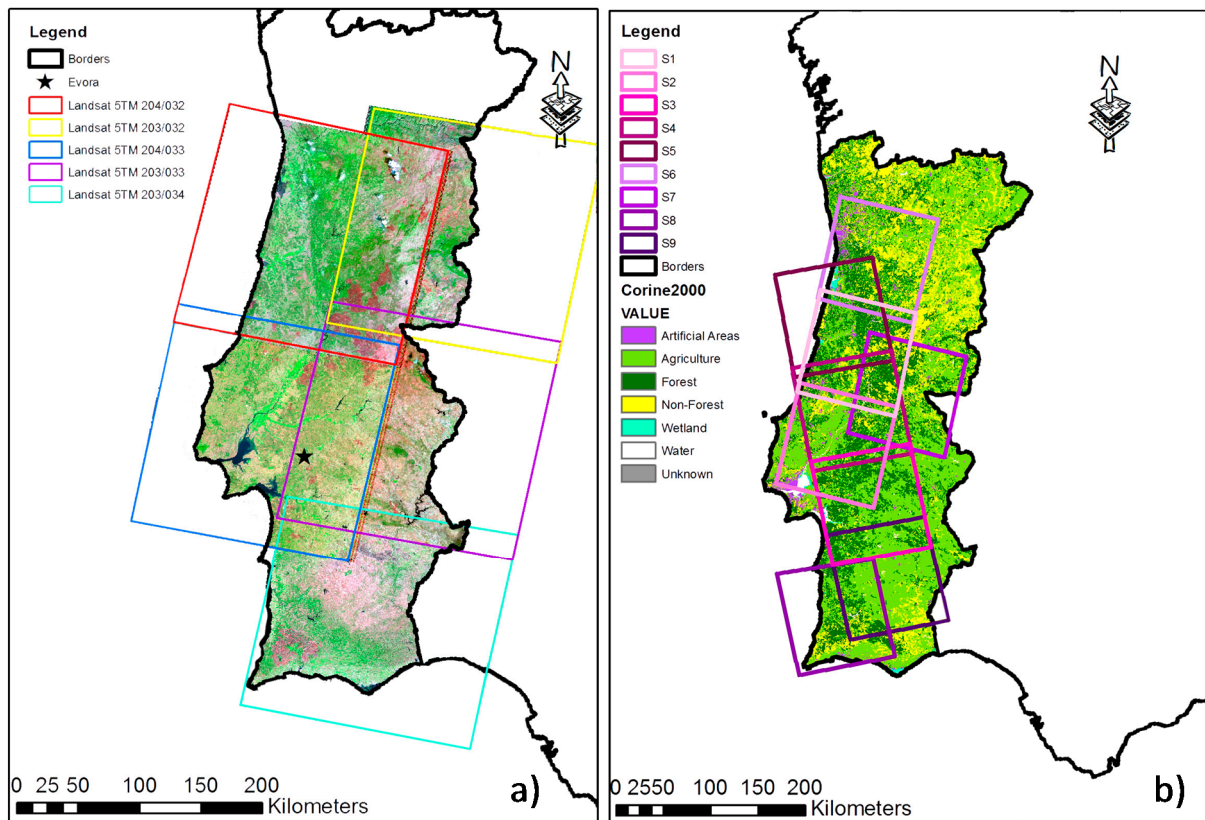


Figure 1. Optical and SAR datasets acquired during the year 2003 and used for this study: (a) Landsat-5 TM images shown as false color composite mosaic (R-G-B: 5-4-3); (b) ENVISAT ASAR data frames overlaid on the Corine Land Cover (CLC2006) map. Lists of optical and SAR scenes are given in Tables 1 and 2.

Table 1. The Path/Row, date of acquisition and percentage of forestland cover (according to the CLC2006 map) for each frame of the Landsat-5 TM data set. The locations of the TM frames are visualized in Figure 1a.

Path/Row	Acquisition Date	Forest Cover (%)
203/032	8 October 2003	28%
203/033	9 June 2003	43%
203/034	24 October 2003	26%
204/032	12 August 2003	19%
204/033	12 August 2003	28%

3.2. ENVISAT-ASAR Images

Information derived from the optical-based analysis has been complemented by the SAR data acquired at C-band (wavelength of ~5.6 cm) by the ASAR sensor onboard the ENVISAT satellite, specifically by collecting over each of the available nine ASAR data frames shown in Figure 1, one pre- and one post-fire season SAR image for the year 2003. SAR data have been acquired in the single VV polarization, imaging mode (IM), and in a Single Look Complex (SLC) format. Pixel spacing of

SLC SAR images is of about $20 \text{ m} \times 5.5 \text{ m}$ (ground range/azimuth). Details of the ASAR dataset are given in Table 2 along with the precipitation cumulated in the four days prior to ENVISAT overpass.

Table 2. SAR data set and pertinent rainfall data.

Frame	Track	Orbit	Name	Acquisition Date	Pass	Cumulated Precipitation * (mm)
2498	452	5516	s1	21 March 2003	Descending	1.76
2494	452	5516	s2	21 March 2003	Descending	14.36
2492	316	6883	s3	24 June 2003	Ascending	0.0
2493	316	6883	s4	24 June 2003	Ascending	0.0
2499	316	6883	s5	24 June 2003	Ascending	0.03
2454	452	5516	s6	21 March 2003	Descending	0.14
3775	180	6246	s7	11 May 2003	Descending	0.0
1377	87	6153	s8	04 May 2003	Ascending	0.11
2497	316	6883	s9	24 June 2003	Ascending	0.0
2496	452	9023	s1	21 November 2003	Descending	0.15
2497	452	9023	s2	21 November 2003	Descending	0.28
2489	316	9388	s3	16 December 2003	Ascending	0.27
2490	316	9388	s4	16 December 2003	Ascending	0.67
2491	316	9388	s5	16 December 2003	Ascending	0.68
2495	452	9023	s6	21 November 2003	Descending	0.31
3774	180	7749	s7	24 August 2003	Descending	0.06
1380	87	8658	s8	16 October 2003	Ascending	8.26
2498	316	9388	s9	16 December 2003	Ascending	0.21

* Source: IPMA, I.P. PT02 gridded precipitation dataset.

SLC SAR images have been co-registered and then averaged by performing a multi-look operation [55] with three looks in range direction and fifteen looks in the azimuth one, resulting in a multilooked SAR pixel spacing of about $60 \text{ m} \times 80 \text{ m}$. Lee noise filter has been applied to multi-looked SLC SAR images. Afterwards, multi-looked amplitude SAR images have been properly geocoded [55], namely converted from radar to UTM projection coordinates and radiometrically calibrated [55,56] to obtain sigma naught (σ°) maps, with a $60 \text{ m} \times 80 \text{ m}$ spatial resolution on the ground. To accurately perform the calibration process of SAR images amplitude, a terrain height correction step was implemented by exploiting the precise satellite orbital information provided by the University of Delft and ASTER GDEM (Advanced Space-borne Thermal Emission and Reflection Radiometer Global Digital Elevation Model) with 30 m spatial resolution. Notice that the ASTER GDEM is the only DEM at 1 arc-second (approximately 30 m) grid with global coverage. The NASA SRTM DEM 1 arc-second data coverage is freely available for only the United States. 3 arc-second data are available for worldwide coverage. ASTER GDEM has been checked for artifacts and the minimum and maximum values occurring in the study areas have been evaluated. The temporal variation of backscattering ($\Delta\sigma^{\circ}_{\text{post-pre}}$) for the 2003 season has been computed starting from the pre- and post-fire (geocoded) σ° maps over the available nine SAR data frames. The SAR image pre-processing steps are shown in Figure 2.

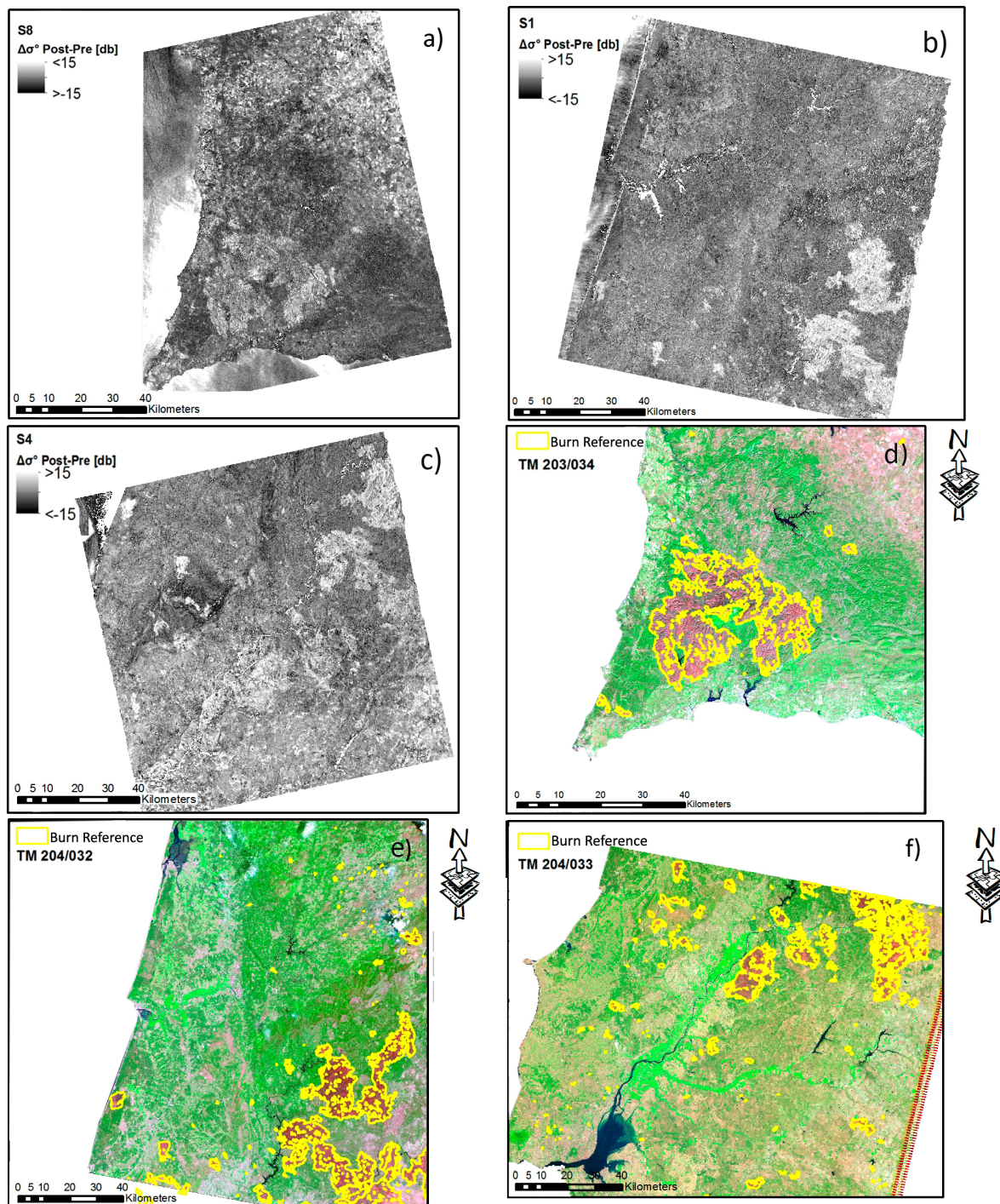


Figure 2. (a,b,c) Over sites s8, s1 and s4 the $\Delta\sigma^\circ$ maps and (d,e,f) the post-fire Landsat-5 TM false color composite (R-G-B 5-4-3) images.

Since the temporal difference between pre- and post-fire images enhances the separability between unburned and burned surfaces [28,57], $\Delta\sigma^\circ_{\text{post-pre}}$ was selected as input to the fuzzy burned area algorithm. The pre-fire season acquisition dates are assumed to be 21 March 2003 (sites s1, s2 and s6), 4 May 2003 (s8), 11 May 2003 (s7) and 24 June 2003 (s3, s4, s5 and s9) while the post-fire season dates are 24 August 2003 (s7), 16 October 2003 (s8), 21 November 2003 (sites s1, s2, s6) and 16 December 2003 (s3, s4, s5, s9). Figure 3 shows $\Delta\sigma^\circ$ maps and Landsat-5 TM false color composite images (R-G-B 5-4-3) over sites s1, s4 and s8. Notice that the burned areas appear as the brighter areas

in the $\Delta\sigma^\circ$ maps and the dark red regions in the TM false color composite images. For convenience, in the rest of the manuscript $\Delta\sigma^\circ$ will denote the (post-pre) variation of σ° .

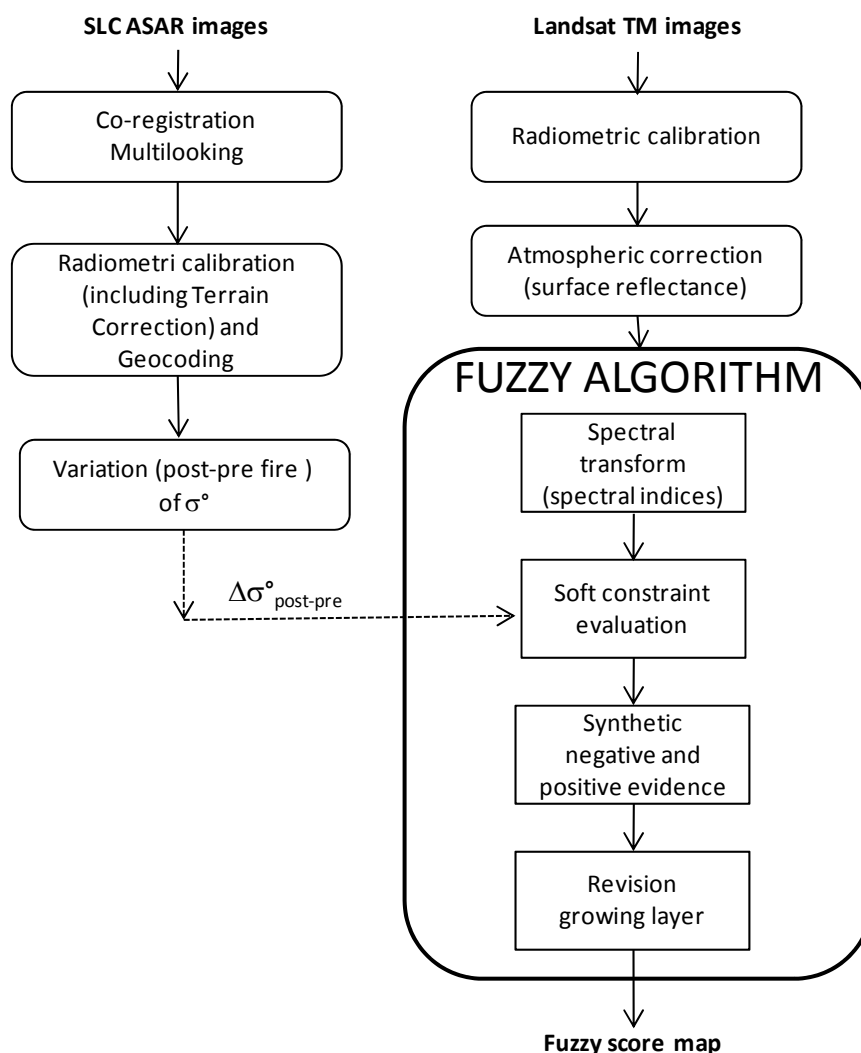


Figure 3. Flowchart of the pre-processing and classification steps implemented for the integration of SAR and optical data in the fuzzy burned area-mapping algorithm.

3.3. Ancillary Datasets

The Corine Land Cover map for the year 2006 (CLC2006) has been obtained from the European Environmental Agency website [52], as a raster dataset with a spatial resolution of $100\text{ m} \times 100\text{ m}$ providing information on the major land cover types over Europe. Figure 1b shows the level 1 land-cover classes over Portugal: artificial surfaces, agricultural areas, forest and semi-natural areas, wetlands and water bodies. The CLC2006 map has been used to derive for each TM frame a mask of those surfaces which are not likely to be affected by fires (also called “unburnable surfaces”) and identified by the following classes: artificial surfaces (level 1 CLC2006 codes 1–10), wetlands (level 1 CLC2006 codes 34–38) and water bodies (level 1 CLC2006 codes 39–43).

Reference burned area perimeters have been extracted from the Landsat based Fire Atlas of Portugal [58] and used for accuracy assessment of the fuzzy burned area maps. This dataset provides

burned area polygons over the entire Portugal for each fire season and it is produced with a semi-automatic classification of Landsat satellite imagery with a minimum mapping unit of 35 ha for the 1975–1983 period (Landsat MSS era) and 5 ha since 1984 (Landsat TM/ETM+ era). A detailed description of the Fire Atlas can be found in Oliveira *et al.* [50]. In this work, the reference fire polygons have been edited to discard burned areas caused by fires occurred later than the post-fire TM acquisitions over the study area.

4. Methods

Figure 3 shows the flowchart of the steps implemented for data pre-processing and image classification (thicker black box). Pre-processing of optical and SAR data are described in Sections 3.1 and 3.2, respectively, whereas the details on the implementation of the fuzzy burned area-mapping algorithm are provided in this section. As shown in Figure 3, the $\Delta\sigma^\circ$ and surface reflectance Landsat-5 TM images constitute input data for the fuzzy algorithm [46,47,59].

The algorithm was initially proposed to map burned areas in Mediterranean regions from Landsat TM/ETM+ data. It is theoretically based on the concept of burn evidence reinforcement [47]: spectral indices derived from the multi spectral bands of the TM/ETM+ sensors can provide consistent coherent information over burned areas, whereas they may have a complementary, incoherent behavior over confusing surfaces (e.g., cloud and topographic shadows, sparse unburned vegetation, and wetlands). The approach relies on the fuzzy integration of the spectral indices and a region-growing algorithm for mapping the areas likely to be burned. In the proposed method, the six spectral indices listed in Table 3 [60–66] have been used. The evidence of burn given by each index (named “partial positive evidence”, PE) is quantified by using fuzzy membership functions as defined by Stroppiana *et al.* [47]. These functions return a fuzzy membership score in the range [0, 1], which also absolves the task to rescale the indices to a unique common domain. In the same way, the indices can be interpreted as a “partial negative evidence” of burn (NE).

The partial positive evidence brought by all indices is integrated in a synthetic score by using Ordered Weighted Averaging (OWA) operators [67,68]. OWAs constitute a parameterized family of soft-mean-like aggregation operators suitable to formalize the expert’s attitude in decision-making problems. In the algorithm, two OWA operators were chosen to derive the layers used for seed selection and region growing, respectively: requiring a high reliability for the seeds, a conservative integration approach and a more relaxed criterion for region growing were used. Partial negative evidence brought by optical indices is integrated in a synthetic layer of negative evidence, which is subtracted to the integrated positive evidence to reduce the unlikely positive evidence over confusing surfaces. Integration of SAR data is carried out at this level: $\Delta\sigma^\circ$ is converted into fuzzy scores (partial negative evidence, $NE_{\Delta\sigma^\circ}$) to be subtracted to the synthetic positive evidence brought by the optical indices and used as seed layer to reduce erroneously selected seeds. Stroppiana *et al.* [47] provide further details of the fuzzy burned area algorithm.

4.1. Membership Function of the Fuzzy Sets for σ° Variation

The fuzzy burned area-mapping algorithm relies on the definition of the membership functions of fuzzy sets (μ) for each input (*i.e.*, the optical spectral indices and the backscatter difference) to

determine the degrees of partial positive/negative evidence (fuzzy scores). The membership functions of the spectral indices originally defined by Stroppiana *et al.* [47] were maintained for this work. Hence, the first step is to define a membership function of fuzzy sets on the domain of the backscattering variation ($\mu_{\Delta\sigma^\circ}$). As for the spectral indices in Stroppiana *et al.* [47], $\mu_{\Delta\sigma^\circ}$ was defined with a partially data-driven approach [69], *i.e.*, based on the analysis of the statistics (average and standard deviation), separability (M , Equation (1)) and frequency distribution of $\Delta\sigma^\circ$ over burned and unburned surfaces. For the analyses provided here, training pixels over burned and unburned surfaces (unburned forest vegetation, soil, and artificial surfaces) have been selected by photo-interpretation of false color composite RGB (5-4-3, 7-4-3) Landsat TM images and used for computing statistics of $\Delta\sigma^\circ$ and separability [70,71], as follows:

$$M = \frac{|\mu_{i,b} - \mu_{i,u}|}{\sigma_{i,b} + \sigma_{i,u}} \quad (1)$$

where $\mu_{i,b}$ and $\sigma_{i,b}$ the mean and standard deviations of the burned surfaces, respectively, and $\mu_{i,u}$ and $\sigma_{i,u}$ are the mean and standard deviations of the unburned surfaces, respectively. Using M we can discriminate between two (burned and unburned) classes. M -separability ranges between 0 (low separability) and ∞ (highest separability): $M > 1.0$ indicates good separation, while $M < 1.0$ stands for poor separation (high histogram overlap). It must be stressed that the two classes are practically separated when $M \gg 1$.

Table 3. The spectral indices used in the fuzzy burned area-mapping algorithm.

Index Name	Formula	Reference
Char Soil Index	$CSI = \rho_4 / \rho_5$	[60]
Enhanced Vegetation Index	$EVI = G * (\rho_4 - \rho_3) / (\rho_4 + C_1 * \rho_3 - C_2 * \rho_1 + 1)$	[61]
Two-band EVI	$EVI2 = G * (\rho_4 - \rho_3) / (\rho_4 + C_3 * \rho_3 + 1)$	[62]
Mid-Infrared Burn Index	$MIRBI = 10 * \rho_7 - 9.5 * \rho_5 + 2$	[63]
Normalized Burn Ratio	$NBR = (\rho_4 - \rho_7) / (\rho_4 + \rho_7)$	[64]
Normalized Burn Ratio 2	$NBR2 = (\rho_5 - \rho_7) / (\rho_5 + \rho_7)$	[64]
Normalized Difference Vegetation Index	$NDVI = (\rho_4 - \rho_3) / (\rho_4 + \rho_3)$	[65]
Soil Adjusted Vegetation Index	$SAVI = (\rho_4 - \rho_3)(1 + L) / (\rho_4 + \rho_3 + L)$	[66]

ρ_i is the surface reflectance in TM bands 1, 2, ... to 7 and $C_1 = 6$, $C_2 = 7.5$, $C_3 = 2.4$, $G = 2.5$, $L = 0.5$.

4.2. Integration of the SAR Membership Function of the Fuzzy Sets for $\Delta\sigma^\circ$

The fuzzy partial negative evidence $NE_{\Delta\sigma^\circ}$ has been integrated with the partial negative evidence from the spectral indices (NBR and MIRBI) [72], to derive a synthetic layer of negative evidence (NE). This layer is used to revise the seed layer to reduce the likelihood of choosing false seeds input to the region growing algorithm as follows: $rPE_{seed} = PE_{seed} - NE$ (PE = Positive Evidence, NE = Negative Evidence, rPE = revised Positive Evidence). In the case of only optical data, $NE = \max(NE_{MIRBI}, NE_{NBR})$ (*i.e.*, negative evidence is given only by optical spectral indices), while in the case of integration optical + SAR by $NE = \max(NE_{MIRBI}, NE_{NBR}, NE_{\Delta\sigma^\circ})$. The region growing

algorithm is the last step to extract the fuzzy score map, which takes values in the range [0, 1]. Finally, a burned area map (0/1 unburned/burned) is derived by applying a threshold to the fuzzy score map.

4.3. Accuracy Assessment

In order to evaluate the performance of the proposed approach, the burned area maps, obtained by employing both optical and SAR data, have been compared with the corresponding ones identified by the reference (burned) polygons, specifically by computing confusion matrices, overall accuracy, commission and omission errors and Kappa coefficient of agreement [73]. Notice that, however, in our case overall accuracy could be biased considering the significant difference between the size of the two classes (burned and unburned).

5. Results and Discussion

5.1. Backscattering Variation over Unburned and Burned Areas

Box-plots in Figure 4 show $\Delta\sigma^\circ$ statistics (median, interquartile range, maximum and minimum values and outliers) for the different surface classes (burned, soil/sparse vegetation, urban and unburned vegetated surfaces) and SAR frames (s1–s9). For each site, *separability* (M) has been evaluated for three different class pairs: burned-soil/sparse vegetation, burned-urban, and burned-unburned forest vegetation (Table 4). Note that values of $\Delta\sigma^\circ$ over burned areas are generally greater than the corresponding ones relevant to unburned surface classes (average = 3.0 ± 1.6 db, all sites together), in agreement with previous findings obtained for Mediterranean environments [19]. Notice that, over site s7 (for which the post-fire acquisition is concomitant to the driest conditions), the fire-event had minor effect on the radar backscattering variation (average $\Delta\sigma^\circ = 0.75$ db) providing the lowest separability values (see Table 4). As far as sites s3, s8 and s9 are concerned, an increasing of $\Delta\sigma^\circ$ also for the soil/sparse vegetation class was observed, thus leading to low separability values (0.06–0.56). It is noteworthy that s5 is the only site that shows a separability greater than 1 for burned/unburned pair comparisons. Despite the generally low separability, it is also worth noting that in the fuzzy algorithm $\Delta\sigma^\circ$ is exploited as negative evidence (conveying information on where the surface is not burned) and combined with information brought by the optical spectral indices (being one source of information among the multiple and complementary inputs).

Results highlight a variability in the behavior of $\Delta\sigma^\circ$ across sites, depending on several factors. First and foremost, the actual scattering patterns naturally exhibit a certain dependence on the local incidence angle, as shown in Tanase *et al.* [25]. Nonetheless, in our case, this effect can be reduced by the use of the (temporal) difference of radar backscattering. Soil moisture has been recognized as an important factor in determining changes in the electromagnetic backscattering. Particularly, in boreal forests Bourgeau-Chavez *et al.* [15] observed an increase of the backscattering after a fire event due to albedo decrease, permafrost melting and evapotranspiration decrease [20].

Different behaviors have been observed for Mediterranean and tropical environments. Since the occurrence of precipitation events can significantly affect the backscattering signature, SAR acquisitions during the wet season are generally characterized by higher backscattering compared to the ones acquired during the dry season [15,23,25].

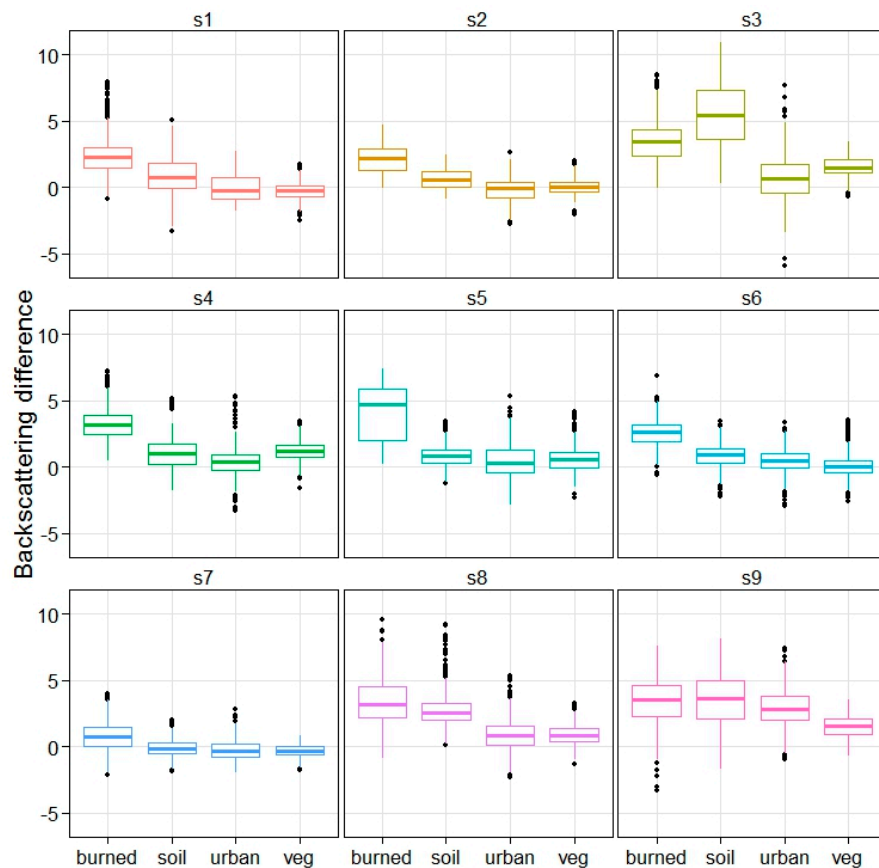


Figure 4. Boxplots (median, interquartile range, maximum and minimum values and outliers) of $\Delta\sigma^\circ$ (dB) for burned, soil/sparse vegetation, urban and unburned vegetation surfaces over the SAR frames s1–s9.

Table 4. The *separability*, M , between burned and different unburned surface classes (soil/sparse vegetation, urban and unburned vegetation) and for the SAR frames (s1–s9), and the number of pixels in the training set (in brackets). The average separability is shown in the last column.

Class	s1	s2	s3	s4	s5	s6	s7	s8	s9	Average
Soil	0.59 (320)	0.79 (376)	0.56 (812)	0.97 (752)	1.16 (782)	0.90 (866)	0.45 (404)	0.20 (614)	0.06 (1049)	0.63
Urban	0.98 (95)	1.15 (454)	0.90 (725)	1.29 (942)	1.11 (867)	1.11 (717)	0.51 (377)	0.87 (617)	1.33 (1088)	1.03
Vegetation	1.33 (428)	1.19 (290)	0.88 (783)	1.07 (915)	1.18 (952)	1.34 (940)	0.66 (409)	1.03 (660)	0.78 (1134)	1.05
Burned	(1311)	(342)	(830)	(864)	(823)	(941)	(382)	(622)	(1064)	-

In other cases (e.g., site 9), the observed $\Delta\sigma^\circ$ could also be explained in terms of fire severity as suggested by Kalogirou *et al.* [44]. These considerations, therefore, underline the key importance of information on environmental variables for understanding the backscattering variation over burned areas [35–39]. Nonetheless, a quantitative and detailed analysis of their influence is outside the scope of this work, since it demands more extensive investigations on heterogeneous environments.

Figure 5 shows the $\Delta\sigma^\circ$ histograms for burned (red) and unburned areas (unburned forest, soil/sparse vegetation, urban all together) (light green) extracted from the training dataset. Based on the above-discussed results, the fuzzy membership function of the negative evidence for the $\Delta\sigma^\circ$ ($\mu_{\Delta\sigma^\circ}$ is defined as follows:

$$\begin{cases} \text{if } \Delta\sigma^\circ \leq 0.0 \Rightarrow NE_{\Delta\sigma^\circ} = 1.0 \\ \text{if } \Delta\sigma^\circ > 3.0 \Rightarrow NE_{\Delta\sigma^\circ} = 0.0 \\ \text{otherwise } NE_{\Delta\sigma^\circ} = -0.33 \times \Delta\sigma^\circ + 1.0 \end{cases} \quad (2)$$

where $NE_{\Delta\sigma^\circ}$ is the negative evidence from $\Delta\sigma^\circ$.

The function defined by Equation (2), used to extract the evidence of unburned conditions, takes value 0 when $\Delta\sigma^\circ > 3$ dB (*i.e.*, over pixels pertinent to a burned areas, degree of membership = 0) and value 1 when $\Delta\sigma^\circ < 0.0$ dB (*i.e.*, over pixels pertinent to unburned areas, degree of membership = 1), given that fires generally induce an increase of the radar backscattering. Intermediate $\Delta\sigma^\circ$ values are linearly scaled between 0 and 1. Similarly to the negative evidence defined for the optical indices (MIRBI and NBR), as proposed in the original version of the algorithm [47], the negative evidence for microwave index $\Delta\sigma^\circ$ is then introduced.

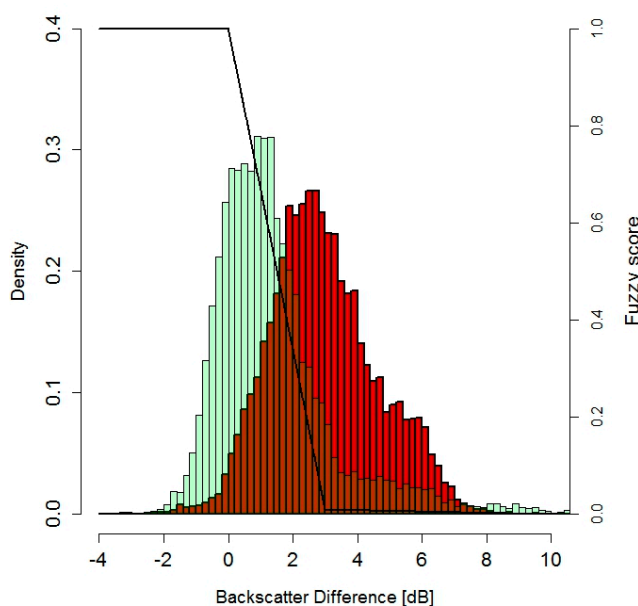


Figure 5. The histograms of $\Delta\sigma^\circ$ values over burned (red) and unburned (green) surfaces (unburned vegetation, soil/sparse vegetation and urban all together) shown as probability density. On the secondary y-axis the score given by the membership function of fuzzy sets ($\mu_{\Delta\sigma^\circ}$ for the negative evidence as defined by Equation (2)).

5.2. Fuzzy Burned Area Maps

The fuzzy score map takes values in the range [0,1] and results from the integration of the membership degrees of positive and negative evidence (brought by NBR and MIRBI optical spectral indices and $\Delta\sigma^\circ$), and the region growing algorithm. Figure 6 shows the fuzzy score map (a) and the reference burned areas (b) extracted from the Landsat Based Fire Atlas of Portugal. In Figure 6a, color keys represent potentially burned areas (fuzzy score > 0), whereas white areas identify unburned surfaces

(fuzzy score = 0). A binary burned area map (0-unburned, 1-burned) can be derived by applying a threshold to the fuzzy score map of Figure 6a. Although the continuous values of the fuzzy score could provide additional information on the conditions of the burned surface (e.g., burn severity), it is necessary to set a threshold value for validation purposes. As a general remark, the two maps show a good agreement, with the exception of some regions along the western coast and in southern Portugal characterized by low fuzzy scores (cyan colors), which are not burned according to the reference dataset.

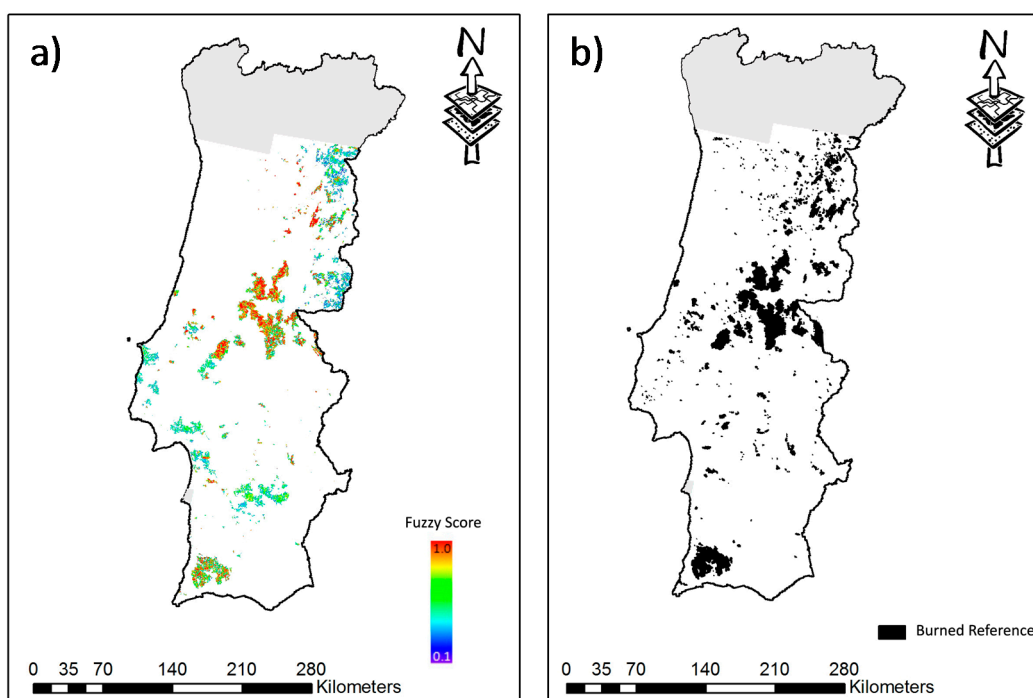


Figure 6. (a) The obtained fuzzy score map; (b) the reference map derived from the Landsat based Fire Atlas of Portugal (where black and white represent burned and unburned areas, respectively).

Figure 7 shows example zoom images over the study area, making visible details that cannot be appreciated at the regional scale of Figure 6, *i.e.*, the output fuzzy score map (column 3) and the input (optical and SAR) data (columns 1 and 2). Notice that the reference fire perimeters (highlighted by the red polygons) are overlaid on the optical RGB false color composite (column 1). It can be observed that actually burned areas are identified by high (yellow to red colors) fuzzy scores (column 3), while low scores correspond to areas that are unlikely to be burned. A clear example is given in panel b where an old burn is adjacent to recent burns and is identified by low fuzzy scores. Moreover, low score regions, which, according to the reference map, are not burned areas, could correspond to the exposed soils. The variability of the fuzzy score could be related to burn severity, although this hypothesis should be further investigated. Finally, Figure 7 highlights the ability of the algorithm to identify the unburned island (fuzzy score = 0, white) within the fire perimeter (e.g., panel c3). The absence of the unburned island in the reference dataset could inflate the commission errors as derived from the confusion matrix.

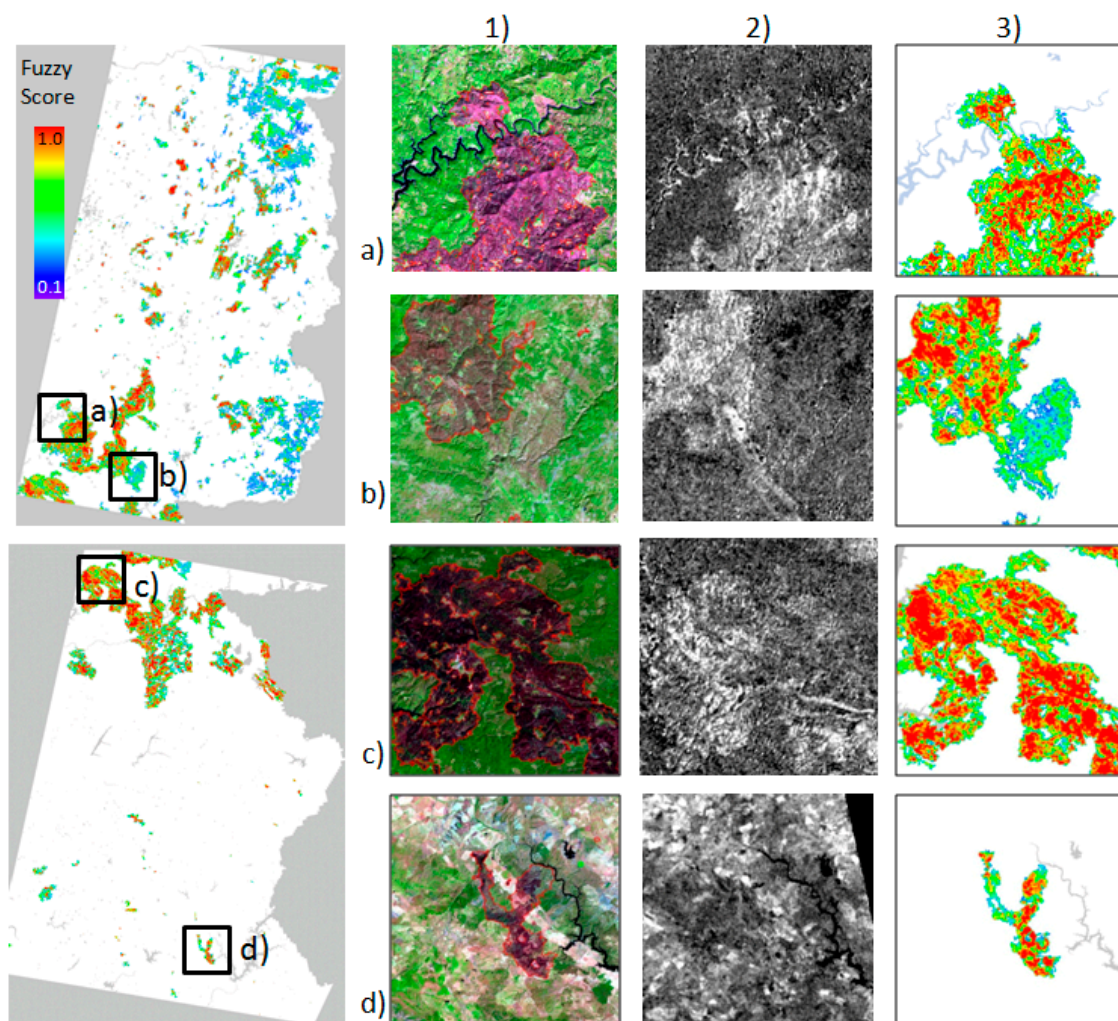


Figure 7. (a–d) Examples of the optical + SAR fuzzy score maps (column 3) over zoom areas of about $22 \text{ km} \times 22 \text{ km}$ from TM frames 203/032 (rows a, b) and 203/033 (bottom) (rows c, d) compared to the Landsat TM (R-G-B 5-4-3) (column 1) and the $\Delta\sigma^\circ$ images (column 2). The red polygons are the reference fire perimeters.

Further investigation was carried out on the variability of the fuzzy score in the map output from the algorithm (Figure 6a) and over actually burned areas as derived from the reference map (Figure 6b) for each TM frame, as well as on the entire study area. Figure 8 shows the histograms the box-plots of the scores in the output fuzzy map and over pixels identified as actually burned in the reference map.

The histograms of the fuzzy scores for pixels belonging to the reference map (green) are biased towards greater values (median for all frames is greater than 0.8) with a significant proportion of values in the $[0.9, 1.0]$ interval, meaning that, over real burns the fuzzy map provides high scores. The white histograms represent the score distribution in the fuzzy map output from the algorithm, where the low scores represent pixels that are likely not to be burned. For example, over frames 203/032 and 204/033, a significant proportion of pixels are assigned low fuzzy scores (white bars in correspondence of low scores), which correspond the regions pointed out in Figure 6a as low score areas (cyan colors). The difference between the two histograms in the range of low score values is an indicator of the

commission error (*i.e.*, areas identified as “burned” but actually “not burned” according to the reference map), which is in fact a function of the threshold applied to the fuzzy score map.

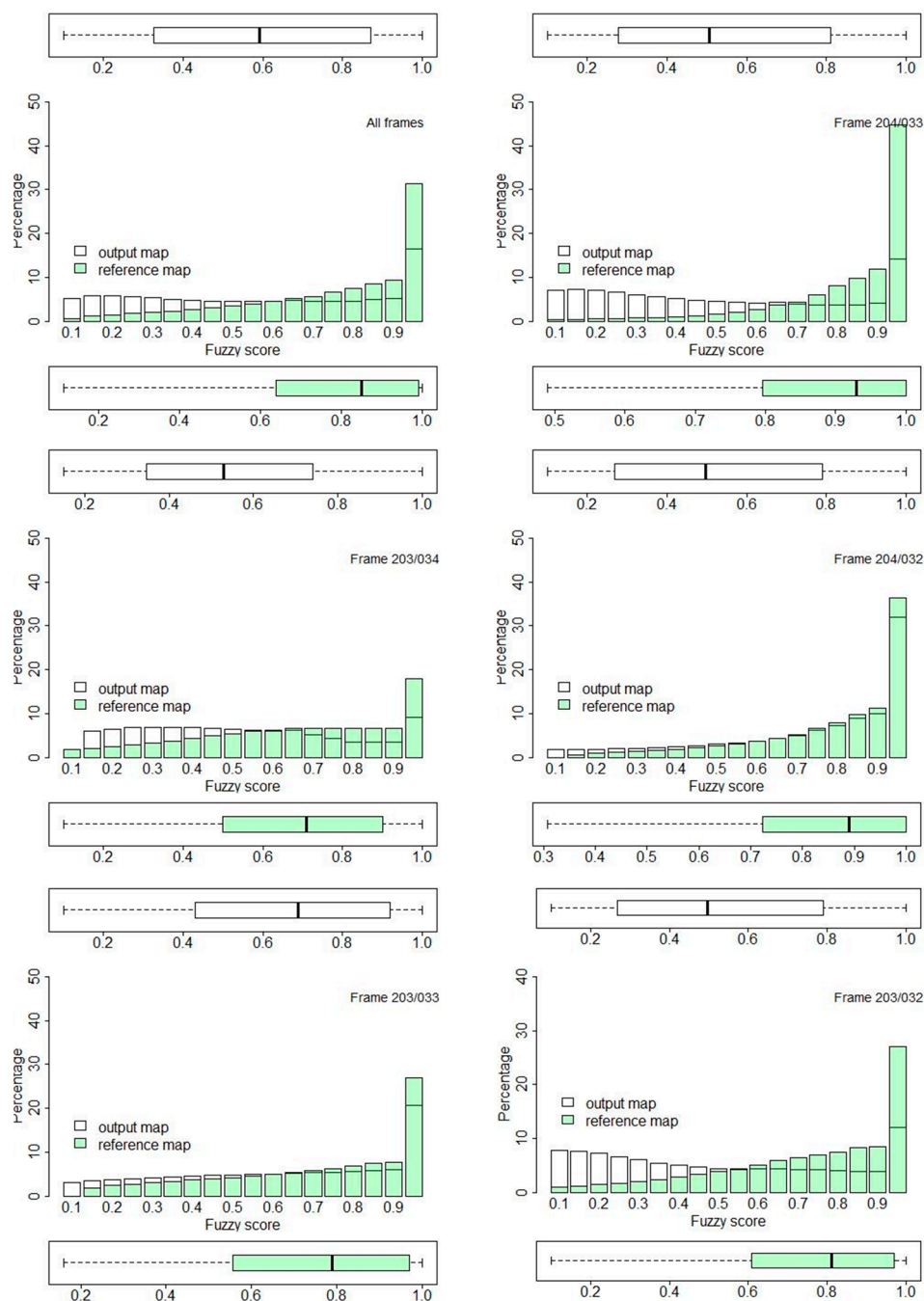


Figure 8. In each panel: the box plot and the histogram (expressed as percentages) of the fuzzy score in the map output from the fuzzy algorithm (white) and over real burned areas as derived from the reference map (green) for each TM frame and the entire study area (“all frames”).

The variability of the burned area map accuracy as a function of the threshold applied on the fuzzy score was analyzed by assessing commission and omission errors and the kappa coefficient for a set of thresholds in the range [0.1, 1.0]. As stated in Section 4, overall accuracy is not a reliable metric for

comparing classes with unbalanced size, and is, therefore, not discussed in this study. Figure 9 shows the omission (OE, light blue triangle markers) and commission errors (CE, red circles) computed from the confusion matrix as a function of the threshold applied to the fuzzy score map for each TM frame and all frames together.

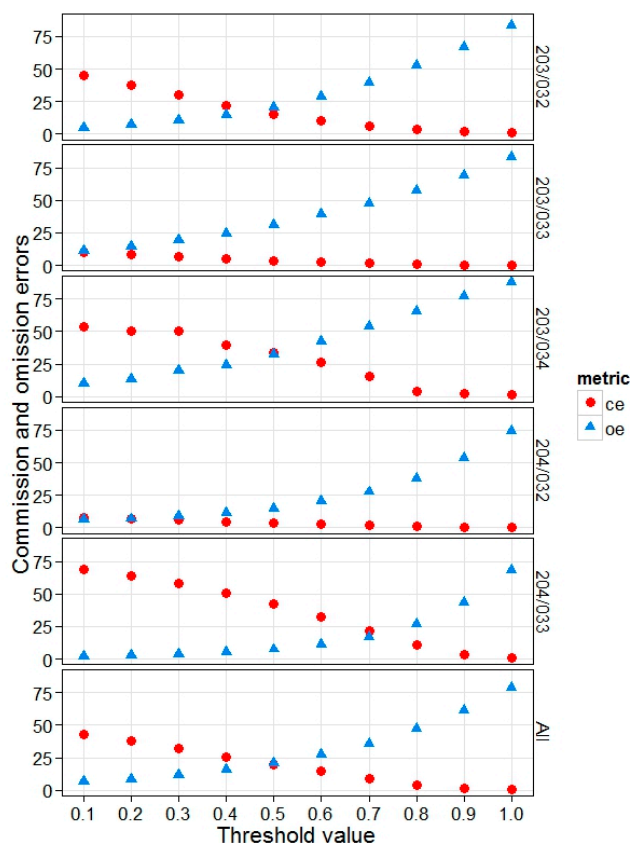


Figure 9. The commission (CE (%), red circle markers) and omission errors (OE (%), blue triangle markers) as a function of the threshold applied to the optical + SAR fuzzy score map (see Figure 6a) for each TM frame and for the study area as a whole (last row).

As expected, low threshold values provide burned area maps with the lowest omission errors ($OE < 10\%$) and the highest commission ($CE > 50\%$) by retaining all the potentially burned areas, including both all actually burned and unburned areas. Increasing the threshold value up to about 0.5 leads to a decrease of the commission error with omission error still lower than 25%: for extreme values of the threshold (> 0.8), CE decreases below 10% but the OE is above 50%. In such a case, the output is conservative, meaning that the areas identified as “burned” are reliable, while several actually burned areas are not identified. Dealing with a binary map (burned/unburned), such a tradeoff between the two types of error is to be expected [74]. Results show that the threshold could be flexibly selected based on user’s requirements on the error levels of the output burned area map. The commission and omission error curves intersect at 0.5. In correspondence to this threshold value the output map provides burned area perimeters with commission and omission errors of 20.1% and 20.8%, respectively, and a kappa coefficient of 0.78 over the study area (Figure 9 bottom row).

5.3. The Role of SAR Data within the Integrated Framework

The results reported above are based on a case study in which the optical data information is not corrupted. This was followed by the analysis of cases in which the information from optical data is affected by artifacts, such as cloud coverage, which emphasizes the effectiveness of the information conveyed by the SAR data.

Figure 10 shows the variability of the commission and omission errors as a function of the threshold applied to the fuzzy score map derived with only optical (red) and optical + SAR data (blue), to point out the contribution of optical-microwave integration. The graphs highlight that integration reduces commission errors without drastically increasing omission. Figure 11 shows the optical + SAR burned area maps derived from the fuzzy score maps by applying a threshold values of 0.1 (top row) and 0.5 (bottom row), where red pixels represent pixels with fuzzy score greater than the threshold value (first column). The optical + SAR accuracy map, *i.e.*, the map showing the spatial distribution of correctly classified burns (orange), omission (blue) and commission errors (green), is shown in the middle column; the last column shows the accuracy map for only optical data.

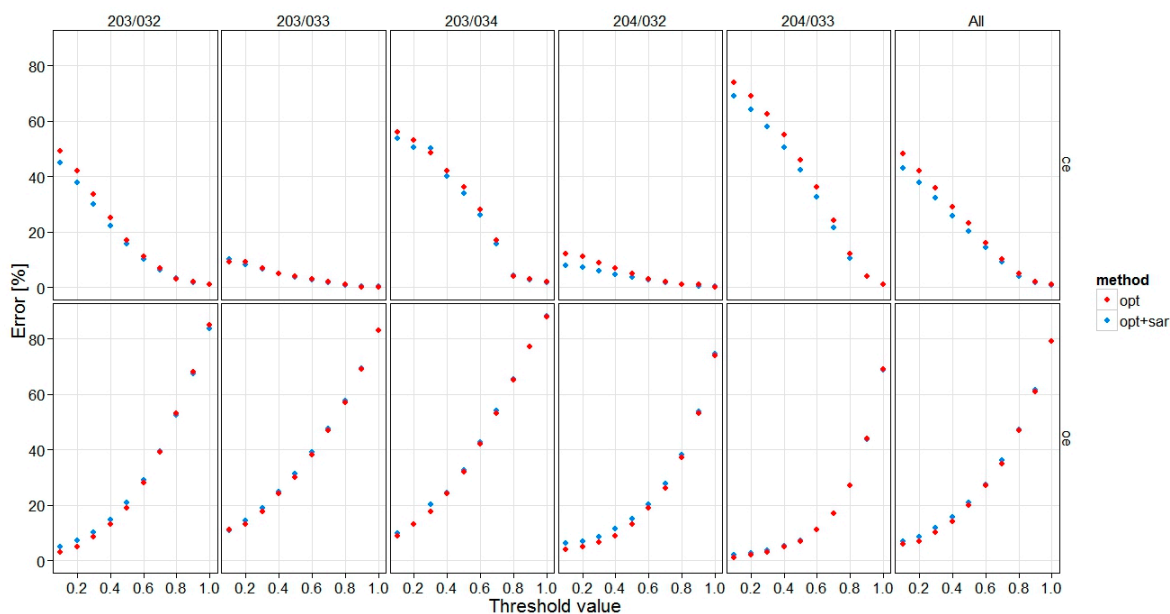


Figure 10. The commission (top row) and omission (bottom row) errors (%) as a function of the threshold applied to the fuzzy score map, derived with only optical (red markers) and optical + SAR data (blue), for each TM frame and for the study area as a whole (last column).

Notice that the commission (omission) errors in the optical + SAR maps are 43.1% (6.8%) and 20.1% (20.8%) for threshold values of 0.1 and 0.5, respectively. On the contrary, in the case in which only optical data are used, the corresponding values of 47.9% (5.7%) and 22.6% (19.6%) are obtained. It is then clear that, by employing clear sky Landsat TM images—as in the considered case—the optical information could already suffice to map burned area. However, the inclusion of SAR information into the algorithm leads to a consistent behavior.

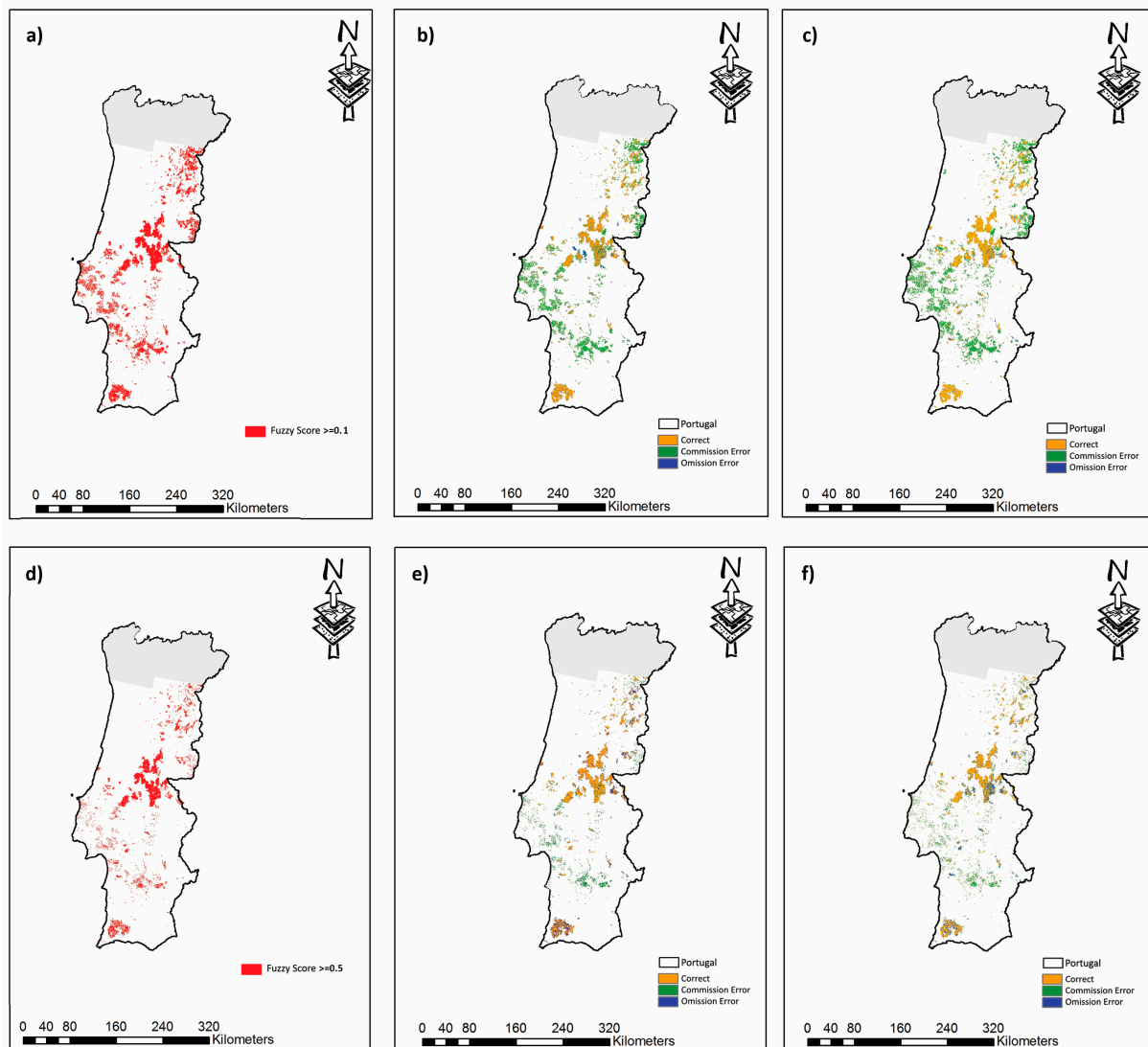


Figure 11. (a–c) the optical + SAR burned area map (first column) and its accuracy map (second column) compared to the accuracy of the burned area map derived with only optical data (third column) in the case of threshold of the fuzzy score 0.1; (d–f) the same for the case of threshold of the fuzzy score 0.5.

When the optical information is poor a significant performance degradation could be observed when only optical data are processed due to the spectral confusion between burned areas and low albedo surfaces [14]. In Figure 12, two examples are considered, where cloud shadows (example 1) and wetlands (example 2) are present and the performance of the algorithm relying only on optical data is poor. However, by complementing it with the SAR contribution, in both cases (d1, d2), a significant reduction of the commission error is obtained, with respect to the case in which only optical data are used (c1, c2). For instance, in the first example, the commission error decreases from 65.4% (optical only) to 11.4% (optical + SAR). These simple examples demonstrate the importance of an integrated framework for processing optical and SAR data for burned area mapping.

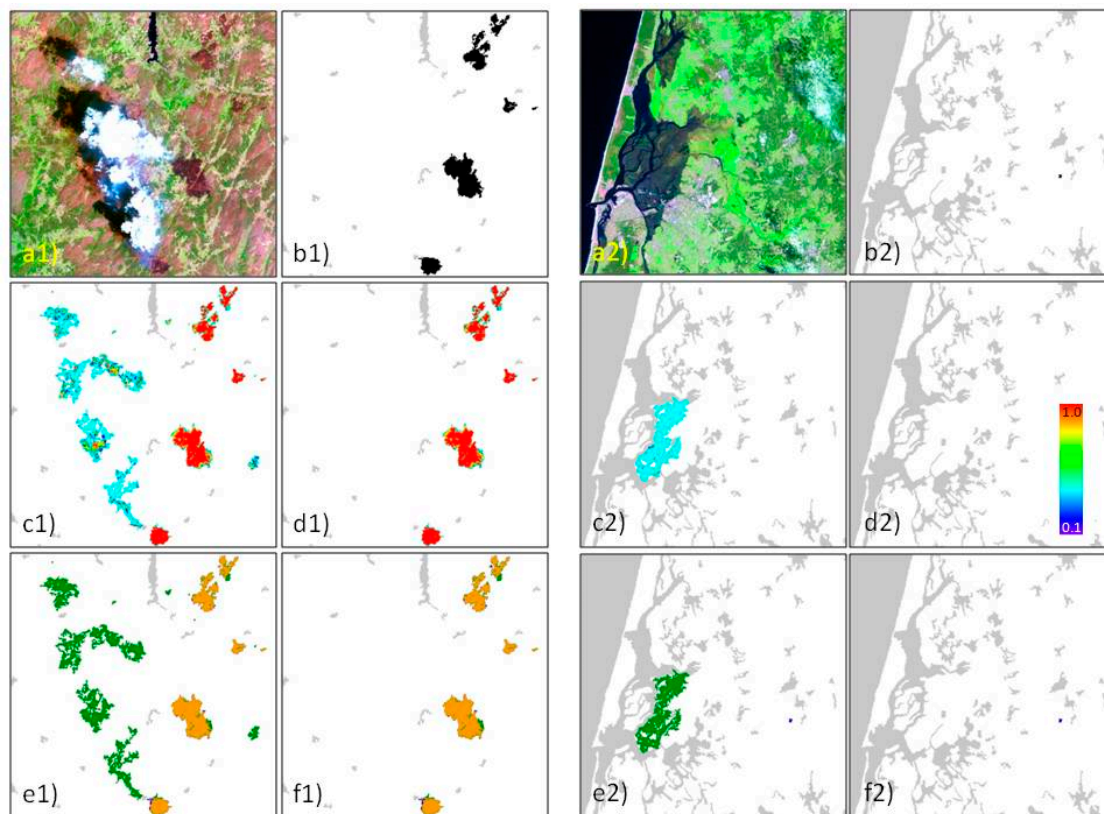


Figure 12. Two cuts relevant to the TM frame 204/032: **(a1,a2)** the false color composite of the TM image (R-G-B 5-4-3); **(b1,b2)** the reference maps (black = burned, white = unburned, grey = masked); **(c1,c2)** the fuzzy score maps obtained with only optical data; **(d1,d2)** the fuzzy score maps obtained with optical + SAR data; **(e1,e2)** the accuracy maps corresponding to (c1,c2); **(f1,f2)** the accuracy maps corresponding to (d1,d2). Each cut covers an area of about 30 km × 30 km.

6. Conclusions

The key importance of the integration of optical and SAR data for fire monitoring to reduce the intrinsic limitations in the exclusive use of optical data has long been recognized. To reduce the commission errors in burned area maps, SAR pre- and post-fire backscatter images ($\Delta\sigma^\circ$) have been integrated into a burned area mapping fuzzy algorithm previously built on the exclusive use of optical data. Being our focus on Mediterranean ecosystems, Landsat-5 TM and ENVISAT ASAR data over Portugal for the year 2003 were acquired and processed. The analysis of $\Delta\sigma^\circ$ images over burned and unburned surfaces has highlighted that, despite the site-specificity of backscattering response, microwave backscattering generally increases after a fire event. Within our framework, a membership function of the fuzzy score for $\Delta\sigma^\circ$ ($\mu_{\Delta\sigma^\circ}$) has been introduced to convey information on unburned areas characterized by no change or decreasing backscattering; these data are exploited as negative evidence of burn in the fuzzy algorithm to reduce seed pixels erroneously identified based solely on the optical spectral indices. The optical + SAR fuzzy score map output from the region growing algorithm provides continuous values in the range (0,1). Although it is necessary to apply a threshold to derive a burned area map (burned = 0, unburned = 1), the fuzzy score could be related to the characteristics of the burned

surfaces, such as for example, burn severity. The commission and omission error levels in the final burned area map are a function of the threshold, which could be flexibly set by the expert based on his/her requirements on the final accuracy. Error levels vary between two extremes: a map where areas identified as burned are highly reliable, *i.e.*, highest user's accuracy (commission error < 5%) and a map where almost all actually burned areas are identified, *i.e.*, highest producer's accuracy (omission error < 10%). An intermediate case, with a 0.5 threshold value, leads to commission and omission errors of about 20% over the study area.

The analysis of the contribution of SAR data to the accuracy of the final burned area map was carried out at the regional and local scales. Results show that $\Delta\sigma^\circ$ images introduced into the fuzzy algorithm can correct for erroneously identified burned areas and thus reduce commission errors. This effect is particularly evident when clear sky optical images are not available (high incidence of cloud shadows) and where low albedo surfaces (e.g., wetlands) are present and not masked out with external information on the land cover. As a consequence, the contribution of the optical + SAR integration can be significant. This result is of particular interest for applications in tropical regions, where cloud cover can be persistent and forest and deforestation fires can produce a significant amount of trace gas emissions due to the high woody fuel load. Further developments could be implemented to exploit the potentiality of SAR data as positive burn evidence, at the same level of the input optical spectral indices. In this perspective, SAR data operatively become an alternative source of information in absence of optical data due to, for example, persistent cloud cover. Moreover, further work will be carried out to investigate the relationship between the fuzzy score and the characteristics of the burned surfaces, such as burn severity. The proposed fuzzy algorithm proved to be flexible and robust and it could be a methodological framework suitable also for testing SAR data acquired at longer wavelength that might provide more separability of the burned surfaces. It will also be suitable for testing data made available by future satellite missions, such as for example, the ESA-Sentinel 1 and 2.

Acknowledgments

ENVISAT ASAR data were provided by European Space Agency (ESA) in the framework of the CAT-1 ESA nr. 11779 project. The authors would like to acknowledge the contribution of M. Bresciani and G. Fontanelli from IREA-CNR, Italy, in data processing and of the anonymous reviewers for their valuable comments.

Author Contributions

Daniela Stroppiana supervised research and algorithm development, carried out the analyses, and prepared the manuscript. Ramin Azar pre-processed remote sensing datasets, run the algorithm, and prepared the graphical contributions. Fabiana Calò, Antonio Pepe and Pasquale Imperatore collected SAR datasets, supervised pre-processing, analyzed and interpreted results, made a significant contribution in writing manuscript. Mirco Boschetti and Pietro A. Brivio proposed the algorithm's theoretical approach, collaborated to algorithm's development, contributed to manuscript writing, editing and revising. João M. N. Silva provided datasets for pre-processing and validation, contributed to the interpretation of the results and to validation, contributed to manuscript writing and revision.

Riccardo Lanari proposed the research design and framework, supervised SAR data pre-processing, revised the manuscript.

Conflicts of Interest

The authors declare no conflict of interest.

References

1. Moreira, F.; Viedma, O.; Arianoutsou, M.; Curt, T.; Koutsias, N.; Rigolot, E.; Barbati, A.; Corona, P.; Vaz, P.; Xanthopoulos, G.; *et al.* Landscape—Wildfire interactions in southern Europe: Implications for landscape management. *J. Environ. Manag.* **2011**, *92*, 2389–2402.
2. Kasischke, E.S.; French, N.H.F.; Harrell, P.; Christensen, N.L., Jr.; Ustin, S.L.; Barry, D. Monitoring of wildfires in boreal forests using large area AVHRR NDVI composite image data. *Remote Sens. Environ.* **1993**, *45*, 61–71.
3. Pereira, J.M.C.; Chuvieco, E.; Karteris, M.; Sousa, A.; Mertin, P.; Koutsias, N. Burnt area mapping in southern Europe using NOAA_AVHRR 1 km satellite mapping burned areas using SMA 661 imagery. In Proceedings of the 3rd International Conference of Forest Fire Research, Coimbra, Portugal, 16–20 November 1998; Volume I, pp. 2667–2677.
4. Barbosa, P.M.; Grégoire, J.-M.; Pereira, J.M.C. An algorithm for extracting burned areas from time series of AVHRR GAC data applied at a continental scale. *Remote Sens. Environ.* **1999**, *69*, 253–263.
5. Chuvieco, E.; Martín, M.P.; Palacios, A. Assessment of different spectral indices in the red-near-infrared spectral domain for burned land discriminations. *Int. J. Remote Sens.* **2002**, *23*, 5103–5110.
6. Mitri, G.H.; Gitas, I.Z. A semi-automated object-oriented model for burned area mapping in the Mediterranean region using Landsat-TM imagery. *Int. J. Wildland Fire* **2004**, *13*, 367–376.
7. Quintano, C.; Fernández-Manso, A.; Fernández-Manso, O.; Shimabukuro, Y.E. Mapping burned areas in Mediterranean countries using spectral mixture analysis from uni-temporal perspective. *Int. J. Remote Sens.* **2006**, *27*, 645–662.
8. Bastarrika, A.; Chuvieco, E.; Martín, M.P. Mapping burned areas from Landsat TM/ETM+ data with a two-phase algorithm: Balancing omission and commission errors. *Remote Sens. Environ.* **2011**, *115*, 1003–1012.
9. Tansey, K.; Grégoire, J.-M.; Stroppiana, D.; Sousa, A.; Silva, J.; Pereira, J.M.C.; Boschetti, L.; Maggi, M.; Brivio, P.A.; Fraser, R.; *et al.* Vegetation burning in the year 2000: Global burned area estimates from SPOT vegetation data. *J. Geophys. Res.* **2004**, *109*, D14S03.
10. Stroppiana, D.; Grégoire, J.-M.; Pereira, J.M.C. The use of SPOT VEGETATION data in a classification tree approach for burnt area mapping in Australian savanna. *Int. J. Remote Sens.* **2003**, *24*, doi:1.1080/01431160210154911.
11. Roy, D.P.; Boschetti, L.; Justice, C.O.; Ju, J. The collection 5 MODIS burned area product—Global evaluation by comparison with the MODIS active fire product. *Remote Sens. Environ.* **2008**, *112*, 3690–3707.

12. Roberts, G.M.; Wooster, J.; Lagoudakis, E. Annual and diurnal african biomass burning temporal dynamics. *Biogeosciences* **2006**, *6*, 849–866.
13. Prins, E.; Schmetz, J.; Flynn, L.; Hillger, D.; Feltz, J. Overview of current and future diurnal active fire monitoring using a suite of international geostationary satellites. In *Global and Regional Wildfire Monitoring: Current Status and Future Plans*; Ahern, F.J., Goldammer, J.G., Justice, C.O., Eds.; SPB Academic Publishing: The Hague, The Netherlands, 2001; pp. 145–170.
14. Pereira, J.M.C.; Sá, A.C.L.; Sousa, A.M.O.; Silva J.M.N.; Santos, T.N.; Carreiras, J.M.B. Spectral characterization and discrimination of burnt areas. In *Remote Sensing of Large Wildfires in the European Mediterranean Basin*; Chuvieco, E., Ed.; Springer-Verlag: Berlin, Germany, 1999; pp. 123–138.
15. Bourgeau-Chavez, L.L.; Kasischke, E.S.; Brunzell, S.; Mudd, J.P.; Tukman, M. Mapping fire scars in global boreal forests using imaging radar data. *Int. J. Remote Sens.* **2002**, *23*, 4211–4234.
16. Liew, S.C.; Kwoh, L.K.; Padmanabhan, K.; Lim, O.K.; Lim, H. Delineating land/forest fire burnt scars with ERS interferometric synthetic aperture radar. *Geophys. Res. Lett.* **1999**, *26*, 2409–2412.
17. Siegert, F.; Hoffmann, A.A. The 1998 Forest Fires in East Kalimantan (Indonesia): A quantitative evaluation using high resolution, multitemporal ERS-2 SAR images and NOAA-AVHRR Hotspot data. *Remote Sens. Environ.* **2000**, *72*, 64–77.
18. Minchella, A.; del Frate, F.; Capogna, F.; Anselmi, S.; Manes, F. Use of multitemporal SAR data for monitoring vegetation recovery of Mediterranean burned areas. *Remote Sens. Environ.* **2009**, *113*, 588–597.
19. Tanase, M.; de la Riva, J.; Santoro, M.; Pérez-Cabello, F.; Kasischke, E. Sensitivity of SAR data to post-fire forest regrowth in Mediterranean and boreal forests. *Remote Sens. Environ.* **2011**, *115*, 2075–2085.
20. French, N.H.F.; Kasischke, E.S.; Bourgeau-Chavez, L.L.; Harrell, P.A. Sensitivity of ERS-1 SAR to variations in soil water in fire-disturbed boreal forest ecosystems. *Int. J. Remote Sens.* **1996**, *17*, 3037–3053.
21. Kasischke, E.S.; Bourgeau-Chavez, L.L.; French, N.H.F. Observations of variations in ERS-1 SAR image intensity associated with forest fires in Alaska. *IEEE Trans. Geosci. Remote Sens.* **1994**, *32*, 206–210.
22. Kasischke, E.S.; French, N.H.F.; Bourgeau-Chavez, L.L. Monitoring of the effects of fire in North American boreal forests using ERS SAR imagery. In *Proceedings of the Third ERS Symposium on Space at the Service of Our Environment*, Florence, Italy, 17–21 March 1997; pp. 363–368.
23. Gimeno, M.; san-Miguel-Ayanz, J. Evaluating of RADARSAT-1 data for identification of burnt areas in Southern Europe. *Remote Sens. Environ.* **2004**, *92*, 370–375.
24. Gimeno, M.; san-Miguel-Ayanz, J.; Schmuck, G. Identification of burnt areas in Mediterranean forest environments from ERS-2 SAR time series. *Int. J. Remote Sens.* **2004**, *25*, 4873–4888.
25. Tanase, M.A.; Santoro, M.; de la Riva, J.; Pérez-Cabello, F.; le Toan, T. Sensitivity of X-, C-, and L-Band SAR backscatter to burn severity in Mediterranean pine forests. *IEEE Trans. Geosci. Remote Sens.* **2010**, *48*, 3663–3675.
26. Tanase, M.A.; Santoro, M.; Aponte, C.; de la Riva, J. Polarimetric properties of burned forest areas at C- and L-Band. *IEEE J. Sel. Top. Appl. Earth Obs. Remote Sens.* **2014**, *7*, 267–276.

27. Polychronaki, A.; Gitas, I.Z.; Veraverbeke, S.; Debien, A. Evaluation of ALOS PALSAR imagery for burned area mapping in Greece using object-based classification. *Remote Sens.* **2013**, *5*, 5680–5701.
28. Bourgeau-Chavez, L.L.; Harrell, P.A.; Kasischke, E.S.; French, N.H.F. The detection and mapping of Alaskan wildfires using a spaceborne imaging radar system. *Int. J. Remote Sens.* **1997**, *18*, 355–373.
29. French, N.H.F.; Bourgeau-Chavez, L.L.; Wang, Y.; Kasischke, E.S. Initial observations of Radarsat imagery at fire-disturbed sites in interior Alaska. *Remote Sens. Environ.* **1999**, *68*, 89–64.
30. Ulaby, F.T.; Moore, R.K.; Fung, A.K. *Microwave Remote Sensing*; Addison-Wesley: Reading, MA, USA, 1982.
31. Voronovich, A.G. *Wave Scattering from Rough Surfaces, Springer Series on Wave Phenomena*; Springer: New York, NY, USA, 1994.
32. Fung, A.K. *Microwave Scattering and Emission. Models and Their Application*; Artech House: Norwood, MA, USA, 1994.
33. Tsang, L.; Kong, J.A.; Shin, R.T. *Theory of Microwave Remote Sensing*; Wiley: New York, NY, USA, 1985.
34. Bass, F.G.; Fuks, I.M. *Wave Scattering from Statistically Rough Surfaces*; Oxford: Pergamon, Greek, 1979.
35. Ishimaru, A. *Wave Propagation and Scattering in Random Media*; Academic: New York, NY, USA, 1993.
36. Luckman, A.J. The effects of topography on mechanism of radar backscatter from coniferous forest and upland pasture. *IEEE Trans. Geosci. Remote Sens.* **1998**, *36*, 1830–1834.
37. Holecz, F.; Wegmuler, U.; Rignot, E.; Wang, Y. Observed radar backscatter from forested areas with terrain variations. In Proceedings of the 1995 Quantitative Remote Sensing for Science and Applications, International Geoscience and Remote Sensing Symposium, Firenze, Italy, 10–14 July 1995; pp. 613–615.
38. Bourgeau-Chavez, L.L.; Kasischke, E.S.N.H.; French, F.L.; Szeto, H.; Kherkher, C.M. Using ERS-1 SAR imagery to monitor variations in burn severity in an Alaskan fire-disturbed boreal forest ecosystem. In Proceedings of the 1994 Surface and Atmospheric Remote Sensing: Technologies, Data Analysis and Interpretation, International Geoscience and Remote Sensing Symposium, Pasadena, CA, USA, 8–12 August 1994; Volume 1, pp. 243–245.
39. Van Zyl, J.J. The effect of topography on radar scattering from vegetated areas. *IEEE Trans. Geosci. Remote Sens.* **1993**, *31*, 153–160.
40. O’Grady, D.; Leblanc, M.; Gillieson, D. Relationship of local incidence angle with satellite radar backscatter for different surface conditions. *Int. J. Appl. Earth Obs. Geoinf.* **2013**, *24*, 42–53.
41. Menges, C.H.; Bartolo, R.E.; Bell, D.; Hill, G.J.E. The effect of savanna fires on SAR backscatter in northern Australia. *Int. J. Remote Sens.* **2004**, *25*, 4857–4871.
42. Siegert F.; Ruecker G. Use of multitemporal ERS-2 SAR images for identification of burned scars in south-east Asian tropical rainforest. *Int. J. Remote Sens.* **2000**, *21*, 831–837.
43. Goodenough, D.G.; Chen, H.; Richardson, A.; Cloude, S.; Hong, W.; Li, Y. Mapping fire scars using Radarsat-2 polarimetric SAR data. *Can. J. Remote Sens.* **2011**, *37*, 500–509.

44. Kalogirou, V.; Ferrazzoli, P.; Della Vecchia, A.; Fomelis, M. On the SAR backscatter of burned forests: A model-based study in C-Band, over burned pine canopies. *IEEE Trans. Geosci. Remote Sens.* **2014**, *52*, 6205–6215.
45. Bernhard, E.-M.; Twele, A.; Gähler, M. Burnt area mapping in the European-Mediterranean: SAR backscatter change analysis and synergistic use of optical and SAR data. In Proceedings of the 2012 International Geoscience and Remote Sensing Symposium, Munich, Germany, 22–27 July 2012; pp. 2141–2143.
46. Boschetti, M.; Stroppiana, D.; Brivio, P.A. Mapping burned areas in a Mediterranean environment using soft integration of Spectral Indices from high-resolution satellite images. *Earth Interact.* **2010**, *14*, 1–20.
47. Stroppiana, D.; Bordogna, G.; Carrara, P.; Boschetti, M.; Boschetti, L.; Brivio, P.A. A method for extracting burned areas from Landsat TM/ETM+ images by soft aggregation of multiple Spectral Indices and a region growing algorithm. *ISPRS J. Photogramm. Remote Sens.* **2012**, *69*, 88–102.
48. Pereira, M.G.; Trigo, R.M.; da Camara, C.C.; Pereira, J.M.C.; Leite, S.M. Synoptic patterns associated with large summer forest fires in Portugal. *Agr. For. Meteorol.* **2005**, *129*, 11–25.
49. Costa, L.; Thonicke, K.; Poulter, B.; Badeck, F.W. Sensitivity of Portuguese forest fires to climatic, human, and landscape variables: Subnational differences between fire drivers in extreme fire years and decadal averages. *Reg. Environ. Chang.* **2011**, *11*, 543–551.
50. Oliveira, S.L.J.; Pereira, J.M.C.; Carreiras, J.M.B. Fire frequency analysis in Portugal (1975–2005), using Landsat-based burnt area maps. *Int. J. Wildland Fire* **2012**, *21*, 48–60.
51. Pereira, J.M.C.; Carreiras, J.M.B.; Silva, J.M.N.; Vasconcelos, M.J.P. Alguns conceitos básicos sobre os fogos rurais em Portugal. In *Em Incêndios Florestais em Portugal: Caracterização, Impactes e Prevenção*; Pereira, J.S., Pereira, J.M.C., Rego, F., Silva, J.M.N., Silva, T.P., Eds.; ISA Press: Lisbon, Portugal, 2006; pp. 133–162.
52. Corine Land Cover Map 2006. Available online: <http://www.eea.europa.eu/data-and-maps> (accessed on 23 January 2015).
53. USGS Glovis Archive. Available online: <http://glovis.usgs.gov> (accessed on 23 January 2015).
54. Vermote, E.F.; el Saleous, N.; Justice, C.O.; Kaufman, Y.J.; Privette, J.L.; Remer, L.; Roger, J.C.; Tanré, D. Atmospheric correction of visible to middle-infrared EOS-MODIS data over land surfaces: Background, operational algorithm, and validation. *J. Geophys. Res.* **1997**, *102*, 17131–17141.
55. Franceschetti, G.; Lanari, R. *Synthetic Aperture Radar Processing*; CRC Press: Boca Raton, FL, USA, 1999.
56. Small, D.; Schubert, A.; Rosich, B.; Meier, E. Geometric and radiometric correction of ESA SAR products. In Proceedings of the ENVISAT Symposium 2007, Montreux, Switzerland, 23–27 April 2007.
57. Azar, R.; Stroppiana, D.; Boschetti, M.; Brivio, P.A.; Pepe, A.; Paglia, L.; Calò, F.; Lanari, R. Integration of optical and SAR remotely sensed data for monitoring wildfires in Mediterranean forests. *Proc. SPIE* **2012**, doi:10.1117/12.974725.
58. Pereira, J.M.C.; Santos, M.T.N. *Fire Risk and Burned Area Mapping in Portugal*; Direcção-Geral das Florestas: Lisbon, Portugal, 2003.

59. Stroppiana, D.; Boschetti, M.; Zaffaroni, P.; Brivio, P.A. Analysis and interpretation of spectral indices for soft multi-criteria burned area mapping in Mediterranean regions. *IEEE Geosci. Remote Sens. Lett.* **2009**, *6*, 499–503.
60. Smith, A.M.S.; Drake, N.A.; Wooster, M.J.; Hudak, A.T.; Holden, Z.A.; Gibbons, C.J. Production of Landsat ETM+ reference imagery of burned areas within Southern Africa savannahs: Comparison of methods and application to MODIS. *Int. J. Remote Sens.* **2007**, *28*, 2753–2775.
61. Huete, A.; Didan, K.; Miura, T.; Rodriguez, E.P.; Gao, X.; Ferreira, L.G. Overview of the radiometric and biophysical performance of the MODIS vegetation indices. *Remote Sens. Environ.* **2002**, *83*, 195–213.
62. Jiang, Z.; Heute A.R.; Didan, K.; Miura, T. Development of a two-band enhanced vegetation index without a blue band. *Remote Sens. Environ.* **2008**, *112*, 3833–3845.
63. Trigg, S.; Flasse, S. An evaluation of different bi-spectral spaces for discriminating burned shrub savanna. *Int. J. Remote Sens.* **2001**, *22*, 2641–2647.
64. Key, C.H.; Benson, N.C. Measuring and remote sensing of burn severity: The CBI and NBR. In Proceedings of the 1999 Joint Fire Science Conference and Workshop, Boise, Idaho, 15–17 July 1999.
65. Rouse, J.W.; Haas, R.H.; Schell, J.A.; Deering, D.W. Monitoring vegetation systems in the Great Plains with ERTS. In proceedings of the Third ERTS Symposium, Washington, DC, USA, 10–14 December 1973; Volume 1, pp. 309–317.
66. Huete, A.R. A soil-adjusted vegetation index (SAVI). *Remote Sens. Environ.* **1988**, *25*, 295–309.
67. Yager, R.R. On ordered weighted averaging aggregation operators in multicriteria decision making. *IEEE Trans. Syst. Man Cyb.* **1988**, *18*, 183–190.
68. Bone, C.; Dragicevic, S.; Roberts, A. Integrating high resolution remote sensing, GIS and fuzzy set theory for identifying susceptibility areas of forest insect infestations. *Int. J. Remote Sens.* **2005**, *26*, 4809–4828.
69. Carrara, P.; Bordogna, G.; Boschetti, M.; Brivio, P.A.; Nelson, A.; Stroppiana, D. A flexible multi-source spatial-data fusion system for environmental status assessment at continental scale. *Int. J. Geogr. Inf. Sci.* **2008**, *22*, 781–799.
70. Kaufman, Y.J.; Remer, L.A. Detection of forests using mid-IR reflectance: An application for aerosol studies. *IEEE Trans. Geosci. Remote Sens.* **1994**, *32*, 672–683.
71. Pereira, J.M.C. A comparative evaluation of NOAA/AVHRR vegetation indexes for burned surface detection and mapping. *IEEE Trans. Geosci. Remote Sens.* **1999**, *37*, 217–226.
72. Stroppiana, D.; Bordogna, G.; Boschetti, M.; Carrara, P.; Boschetti, L.; Brivio, P.A. Positive and negative information for assessing and revising scores of burn evidence. *IEEE Geosci. Remote Sens. Lett.* **2012**, *9*, 363–367.
73. Cohen, J. A coefficient of agreement for nominal scales. *Educ. Psychol. Meas.* **1960**, *20*, 37–46.
74. Boschetti, L.; Flasse, S.P.; Brivio, P.A. Analysis of the conflict between omission and commission in low spatial resolution dichotomic thematic products: The Pareto Boundary. *Remote Sens. Environ.* **2004**, *91*, 280–292.